A Subnanoscale Investigation of Sb Segregation at MnO/Ag Ceramic/Metal Interfaces

Sebastian, Jason T.; Assaban, Albert; Seidman, David N.; Kooi, Bart J.; Hosson, Jeff Th.M. De

Published in:
Ultramicroscopy

Publication date:
2001

INTERFACE SCIENCE 9, 199–211, 2001

A Subnanoscale Investigation of Sb Segregation at MnO/Ag Ceramic/Metal Interfaces

JASON T. SEBASTIAN, ALBERT ASSABAN AND DAVID N. SEIDMAN*
Department of Materials Science and Engineering, Northwestern University, 2225 N. Campus Drive Evanston, IL 60208-3108, USA
d-seidman@northwestern.edu

BART J. KOOI AND JEFF TH. M. DE HOSSON
Department of Applied Physics, University of Groningen, Groningen, The Netherlands

Abstract. We have studied Sb segregation at MnO/Ag(Sb) ceramic/metal heterophase interfaces employing three-dimensional atom-probe (3DAP) microscopy. Specimens are prepared by the internal oxidation of Ag(Mn) alloys, leading to the formation of nanometer-size MnO precipitates within a Ag(Mn) matrix. Sb is introduced into the internally oxidized specimens with a vapor diffusion treatment. Appreciable Sb segregation is observed only after a subsequent segregation anneal is performed, and the measured interfacial excess of Sb at the MnO/Ag(Sb) interfaces, $\Gamma_{Sb}^{MnO/Ag}$, is determined directly. The temporal evolution of the MnO precipitates is followed for the different processing steps employed. It is shown that the concentration of silver within the MnO precipitates decreases from an initial value of 45–50 at.% Ag to less than 5 at.% Ag with increasing annealing time at the different processing temperatures. Thus the MnO precipitates form under paraequilibrium conditions and the precipitates inherit Ag from the matrix. With increasing aging time orthoequilibrium conditions prevail and the MnO precipitates reject the silver atoms they inherited from the matrix.

Keywords: atom probe, field-ion microscopy, ceramics, metals, oxides, interface, segregation

1. Introduction

Ceramic/metal heterophase interfaces play a crucial role in many important technological applications including thermal and corrosion barriers in superalloy turbine blades, microelectronics packaging, and thin film and multilayer devices [1]. In such applications, it is frequently the properties of the heterophase interface, and not of the bulk materials, that dictate the behavior of the system. One of the properties of ceramic/metal interfaces of greatest concern is the interfacial segregation of impurity atoms. The presence of impurity atoms, even in very small concentrations, can change drastically other properties of the interface, for instance, adhesion and electronic properties. The classic example is the exfoliation of Al_2O_3 thermal barriers on Ni-based superalloy turbine blades due to interfacial segregation of sulfur. In this article, we present results on the MnO/Ag(Sb) ceramic/metal interface. A recent investigation of this system determined that the presence of Sb (and also Zn) impurities at ceramic/metal interfaces affects drastically both the morphology and the distribution of precipitates formed upon the internal oxidation of Ag(Mn) alloys [2]. Such an observation highlights the need for studying quantitatively impurity segregation at ceramic/metal interfaces.

Although segregation of impurity species at interfaces is a phenomenon that is ubiquitous in materials science, it is not well understood. In particular, there is a dearth of experimental techniques that allow for the direct, real-space quantification of segregation at

*To whom all correspondence should be addressed.

initially pristine internal interfaces. The technique that shows exceptional promise in tackling this challenging experimental problem, on a subnanometer to nanometer scale, is three-dimensional atom-probe (3DAP) microscopy. 3DAP microscopy [3–5] is a powerful experimental technique that allows for the quantitative and direct measurement of segregation of specific elements at internal interfaces without data deconvolution and without recourse to absolute external standards. The technique relies upon the enhanced electric field at the apex of a sharply polished, needle-shaped specimen to which a high voltage is applied [6]. The strong electric field (on the order of tens of volts per nanometer) results in the field-evaporation of ions from the tip of a specimen in a highly controlled manner. The chemical identities of these ions are determined by time-of-flight mass spectrometry and a two-dimensional position-sensitive detector records the impact positions of the individual ions. The chemical and positional data of each ion is then used to create a three-dimensional atomic reconstruction of the analyzed volume. A typical reconstructed volume has dimensions of 10 nm × 10 nm × 100 nm and includes approximately 500,000 atoms, although data sets of four to five million atoms are readily attainable [7]. The overall detection and positioning efficiency of the 3DAP is approximately 60–65%; that is, 60–65% of the atoms in the specimen are represented in the final atomic reconstruction.

3DAP microscopy has been applied recently to the study of segregation at ceramic/metal interfaces and at metal/metal heterophase interfaces [8–14]; these studies rely on recent advances in 3DAP data analysis. Specifically, we have developed the so-called proximity histogram, or "proxigram," method to quantify the segregation of impurity atoms at topologically complicated interfaces in 3DAP reconstructions [15]. This powerful analysis method allows for the direct determination of the Gibbsian interfacial excess of a segregating species (Γ_s) at such interfaces, independent of their specific topology. In particular, the surfaces need not be flat.

In the current paper, we present results from 3DAP investigations of Sb segregation at MnO/Ag(Sb) ceramic/metal interfaces. Sb is introduced into internally oxidized Ag(Mn) specimens with a vapor diffusion treatment. Significant Sb segregation at the MnO/Ag(Sb) ceramic/metal interfaces is only detected after a segregation anneal is performed at 550°C.

2. Experimental Procedure

Alloys with a nominal composition of Ag – 1 at.% Mn were prepared by arc melting, and 200 μm diameter wires were drawn from the as-cast ingots. The Ag(Mn) wires were then subjected to a three-step internal oxidation treatment: (1) Annealing in vacuum at 550°C for 6 hours; (2) Internal oxidation in air at 900°C for 30 minutes; and (3) Annealing in vacuum at 650°C for 48 hours. Internal oxidation yields a distribution of nanometer-size MnO precipitates in a Ag matrix with a high number density.

To introduce antimony into the internally oxidized specimen wires, a vapor diffusion technique was employed [10, 16]. The wires were placed across the top of an alumina (Al_2O_3) boat containing a small amount of pure antimony and this arrangement was then placed in a vacuum furnace at 700°C for 110 hours. This temperature is above the melting temperature of antimony, allowing Sb to evaporate and diffuse into the internally oxidized Ag(Mn) wires. Under these thermal conditions the value of the dimensionless parameter Dt/a^2 is approximately 1.6, where D is the diffusivity of Sb in Ag [17], t is time, and a is the radius of the wire. Examination of the relevant solution to the diffusion equation (viz. diffusion into a cylinder with a constant surface concentration) shows that for a value of Dt/a^2 greater than approximately 0.8, the concentration of the diffuser within the cylinder is homogenous [18]. Clearly, for the conditions described above, the concentration of Sb within the wires is constant and homogeneous.

After introducing antimony the wires were further annealed at 550°C for 30 hours in vacuum to increase the level of Sb segregation at the internal MnO/Ag ceramic/metal heterophase interfaces. Under these conditions, the minimum root-mean squared diffusion of Sb in Ag, $\sqrt{2Dt}$, is approximately 15.5 μm [17]. This relatively large diffusion distance (with respect to interprecipitate distance, which is on the order of nanometers) ensures that the Sb in the metal matrix is at the very least in local equilibrium with the segregating Sb at the MnO/Ag(Sb) interfaces. The processing procedures used to prepare specimens are displayed in Fig. 1.

Four different specimen groups were therefore created: (A) As-cast; (B) Internally oxidized (without Sb); (C) Internally oxidized containing Sb; and (D) Internally oxidized containing Sb plus a segregation anneal. These different processing treatments are referred to as groups A, B, C and D, respectively. Their characteristics are summarized in Table 1.

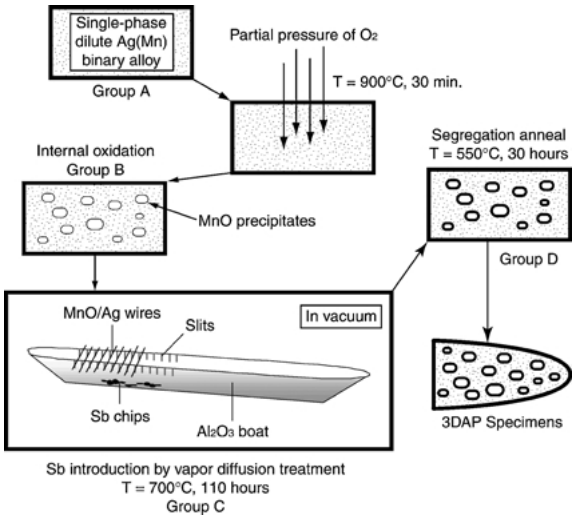

Figure 1. Schematic showing the process of specimen preparation.

Specimens were analyzed utilizing our 3DAP microscope. Field-ion microscopy (FIM) was performed at a specimen temperature of 60 K using argon as the imaging gas; FIM was performed only for tip development and alignment purposes. For atom-probe analyses, a specimen temperature of 45 K, a pulse fraction (ratio of pulse voltage to steady-state dc voltage) of 15%, a pulse frequency of 1500 Hz, and an evaporation rate of between 25 to 50 pulses per ion (0.02 to 0.04 ions per pulse) were employed. These values were based on experimental conditions used in previous two-dimensional atom-probe (2DAP) and 3DAP investigations of internally oxidized Ag alloys [9, 19–21]. Analysis of the 3DAP data was performed using "*Adam*," a custom software program we have developed for 3DAP data rendering and analysis [22].

Table 1. Characteristics of the different types of specimens studied (also see Fig. 1).

Group	Description	Heat treatment
A	As-cast	6 hr. at 550°C (vacuum; recrystallization)
B	Internally oxidized (without Sb)	30 min. at 900°C (air; internal oxidation) 48 hr. at 650°C (vacuum)
C	Internally oxidized with Sb introduction	110 hr. at 700°C (with Sb, vacuum; Sb introduction)
D	Internally oxidized with Sb introduction and segregation anneal	30 hr. at 550°C (vacuum; Sb segregation anneal)

3. Results

3.1. As-Cast Specimens (Group A)

A three-dimensional atom-probe reconstruction of a group A (as-cast) specimen is presented in Fig. 2(a). The corresponding Mn and O concentrations, as functions of analysis depth, are shown in Fig. 2(b). A mass spectrum from this specimen is shown in Fig. 3. All mass spectra presented in this article have been calibrated carefully using a new method we have developed for the calibration of 3DAP mass spectra [23].

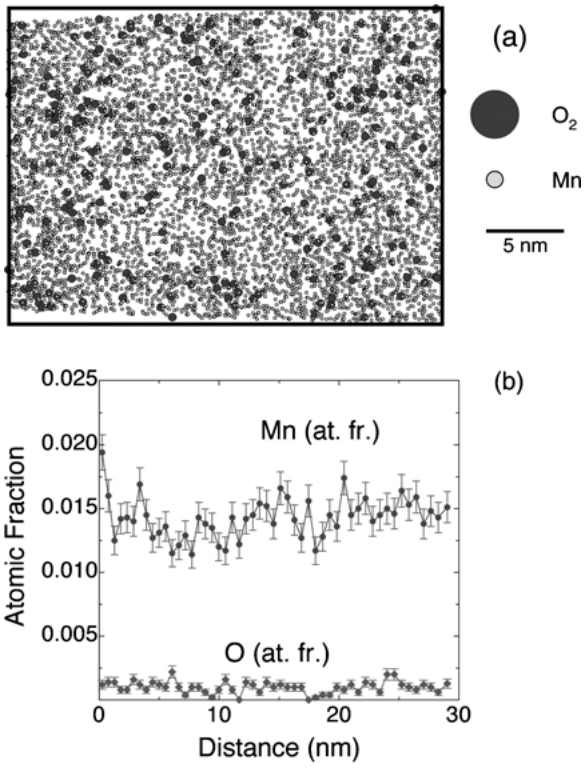

Figure 2. (a) 3DAP reconstruction of an as-cast Ag(Mn) alloy (side view—the analysis direction is left-to-right). The dimensions of the box are $22.9 \times 22.4 \times 29.5$ nm^3; there are 514,025 atoms in the reconstruction. Mn atoms are small and light colored, diatomic oxygen molecules (remnant gaseous oxygen in the 3DAP chamber) are large and dark. The matrix Ag atoms have been omitted for the sake of clarity. (b) Concentration profile showing the Mn and O concentrations as a function of analysis depth (left to right in Fig. 2(a)). An average composition of 1.42 at.% Mn is measured. The error bars represent the $\pm\sigma$ error bounds.

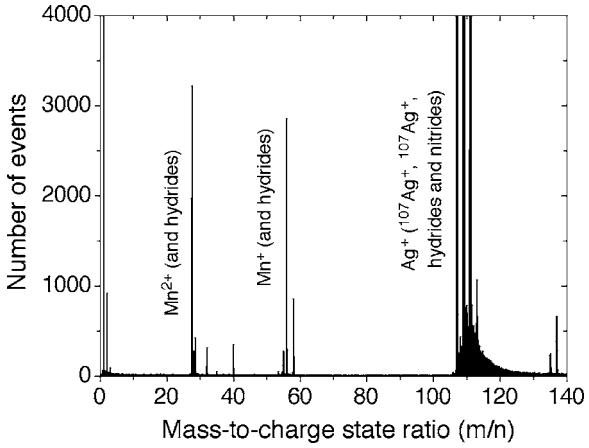

Figure 3. Mass spectrum of an as-cast specimen (group A). The salient groups of peaks are labeled in the figure (the Ag^{+} nitrides are the peaks that are furthest to the right). Furthermore, the peaks at mass-to-charge state ratios of 1 and 2 are residual singly-charged hydrogen (H^{+} and $H_2{}^{+}$), the peak at a mass-to-charge state ratio of 32 is $O_2{}^{+}$, and the peak at a mass-to-charge state ratio of 40 is Ar^{+} (residual imaging gas from FIM).

3.2. Internally Oxidized (without Sb) Specimens (Group B)

A 3DAP reconstruction of a group B (internally oxidized) specimen is presented in Fig. 4(a). The corresponding 16 at.% Mn isoconcentration surfaces, overlaid on the data set, are shown in Fig. 4(b); only the matrix atoms are shown for the sake of clarity. A portion of the mass spectrum of this group B specimen is shown in Fig. 5. Table 2 lists all of the mass spectrum windows used to create the 3DAP reconstructions in Fig. 4(a) and 4(b). Figure 6 shows a proxigram analysis of Mn, O and Ag atomic concentrations as functions of distance to the isoconcentration surface shown in Fig. 4(b). The construction of a proxigram is described further in Section 4.1.

3.3. Internally Oxidized Containing Sb (Group C)

A proxigram that displays the Mn, O, Ag and Sb atomic concentrations as functions of distance to the surfaces of the precipitates of the group C specimen is displayed

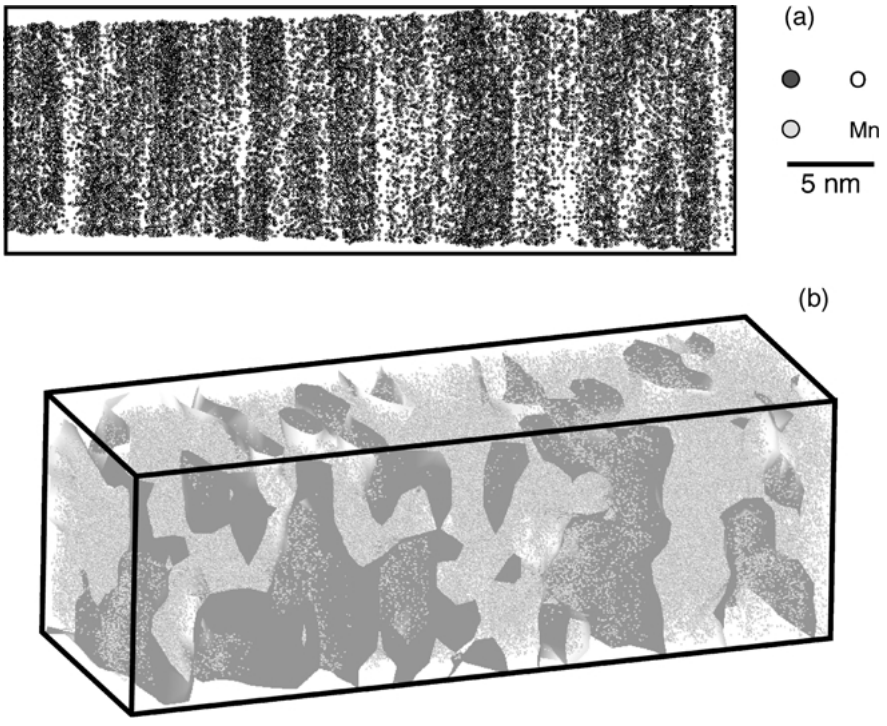

Figure 4. (a) 3DAP reconstruction of an internally oxidized Ag(Mn) alloy (side view—the analysis direction is left to right). The dimensions of the box are $15.3 \times 15.0 \times 44.1$ nm^3; there are 347,388 atoms in this reconstruction. The matrix Ag atoms have been omitted for the sake of clarity. (b) A 16 at.% Mn isoconcentration surface constructed from (a). In this figure the Mn and O atoms are omitted, and only the matrix Ag atoms are shown. It is clear that within the regions bounded by the isoconcentration surfaces, the density of matrix Ag atoms is reduced.

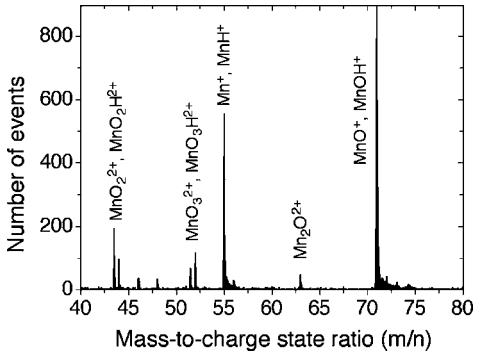

Figure 5. A portion of the mass spectrum of an internally oxidized specimen (see Fig. 4(a) and (b)). The salient groups of peaks are labeled in this figure. We see the presence of a number of complex ionic species, not observed in the spectrum of the as-cast specimen (Fig. 3), that are associated with the field evaporation of the MnO ceramic precipitates.

in Fig. 7. For this group C specimen, 3DAP reconstructions are not shown.

3.4. Internally Oxidized Containing Sb plus Segregation Anneal (Group D)

Figure 8 depicts a 3DAP reconstruction of a group D (internally oxidized containing Sb in solid-solution plus a segregation anneal) specimen. Figure 9(a) shows a proxigram analysis of Mn, O, Ag and Sb concentrations as functions of distance to a 16 at.% Mn isoconcentration surface superimposed on the reconstruction in Fig. 8; the isoconcentration surface used to construct this proxigram has not been shown for Fig. 8 as it was in Fig. 4(b). Figure 9(b) shows a blow up of a portion of the Sb curve in Fig. 9(a), highlighting explicitly the peak corresponding to Sb segregation at the MnO/Ag(Sb) interfaces.

In Fig. 10, a slice from the reconstruction in Fig. 8 has been isolated and is displayed. This slice is taken from approximately the middle of the reconstruction. A 16 at.% Mn isoconcentration surface is overlaid on the reconstruction, delineating the distinction between matrix and precipitate within this small slice (the thickness of the slice is approximately 1 nm).

4. Discussion

4.1. Specimens without Segregation (Groups A, B, and C)

Figure 2(a) and (b) demonstrates that the distribution of Mn atoms is essentially random, with an average concentration of approximately 1.4 at.% (cf. the starting, nominal composition of 1 at.% Mn). The small amount of oxygen depicted in Fig. 2(a) and (b) has its origins in ionized, gaseous (diatomic) oxygen present in the 3DAP analysis chamber, and not dissolved oxygen in the as-cast Ag(Mn) alloy. Examining the mass spectrum of the specimen (Fig. 3), we see that in addition to residual gas peaks (background hydrogen and oxygen from the 3DAP chamber; argon from FIM), only Ag^+, Mn^+ and Mn^{2+} ions, along with their hydrides and some Ag^+ nitrides, are observed. Hydrides and nitrides are formed as a result of chemical reactions, in the high electric field associated with a tip, between the atoms composing a tip and the residual hydrogen and nitrogen gas atoms present in the 3DAP microscope analysis chamber.

Table 2. Mass windows for the group B (internally oxidized) specimen used to create the 3DAP reconstructions in Fig. 4(a) and (b).

Peak identity	Window mass range (amu)	Number of masses before positioning
O^+	15.9 to 16.1	4963
OH^+	16.9 to 17.1	262
Mn^{2+}	27.35 to 27.6	9888
MnH_2^{2+}	28.4 to 28.6	3290
MnH_3^{2+}	28.9 to 29.1	111
MnH_4^{2+}	29.4 to 29.6	627
O_2^+	31.9 to 32.15	886
MnO^{2+}	35.4 to 35.7	291
$MnOH^{2+}$	35.85 to 36.1	532
MnO_2^{2+}	43.3 to 43.65	414
MnO_2H^{2+}	43.85 to 44.1	206
MnO_3^{2+}	51.35 to 51.65	170
MnO_3H^{2+}	51.8 to 52.15	323
Mn^+	54.8 to 55.2	1719
MnH^+	55.9 to 56.1	100
Mn_2O^{2+}	62.8 to 63.2	157
MnO^+	70.8 to 71.2	3029
$MnOH^+$	71.9 to 72.1	133
MnO_2^+	86.8 to 87.2	3465
$MnO_2H_2^+$	88.85 to 89.1	163
MnO_3^+	102.8 to 103.2	4520
$^{107}Ag^+$	106.8 to 107.3	166930
$^{107}AgH_2^+$, $^{109}Ag^+$	108.8 to 109.3	194830
$^{109}AgH_2^+$	110.8 to 111.3	41265
Total		438274

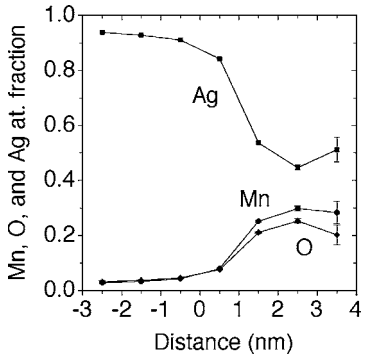

Figure 6. Proxigram showing the atomic fractions of Mn, O, and Ag as a function of distance to the isoconcentration surface in Fig. 4(b). Negative distances represent regions outside of the isoconcentration surface (i.e., matrix); positive distances represent regions inside of the isoconcentration surface (i.e., precipitates). The error bars are large on the rightmost data points due to the limited proxigram bin population for this value of the abscissa. We note approximately a 1:1 stoichiometry within the MnO precipitates. The centers of the precipitates, however, contain, on average, approximately 45 at.% Ag.

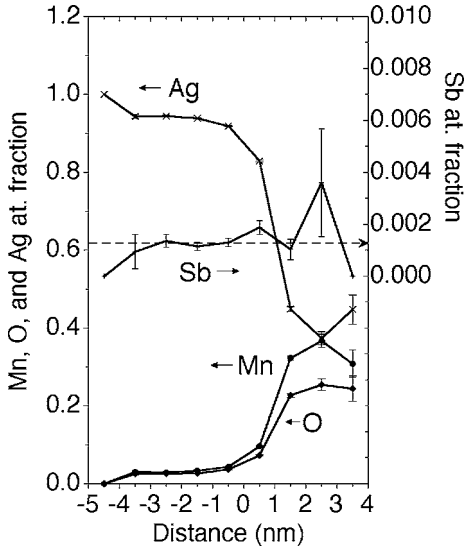

Figure 7. Proxigram showing the Mn, O, Ag and Sb atomic fractions as functions of distance from the surfaces of the precipitates of a group C specimen (for this specimen, the 3DAP reconstructions have not been shown). As with the group B specimen (Fig. 6), we see approximately a 1:1 stoichiometry within the MnO precipitates. Though there appears to be evidence of Sb segregation at the MnO/Ag(Sb) interface, the segregation cannot be considered to be statistically significant (see text for further discussion). The background level of Sb within the Ag matrix is approximately 0.0013 at.fr. (0.13 at.%). The centers of the precipitates contain, on average, approximately 35–40 at.% Ag, which is somewhat reduced relative to the group B specimen (Fig. 6).

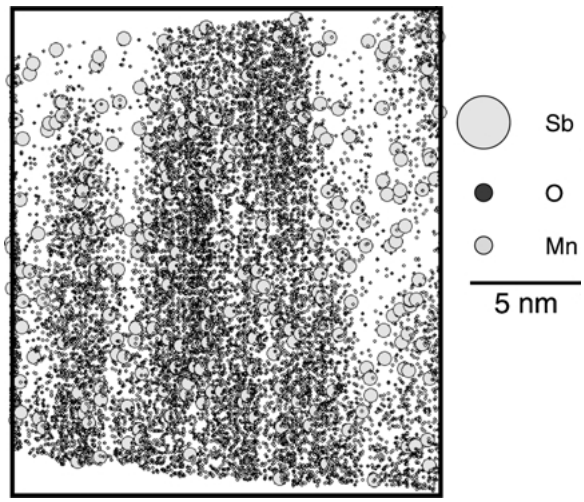

Figure 8. 3DAP reconstruction of an internally oxidized Ag(Mn) alloy containing Sb (side view—the analysis direction is left to right). The Sb was introduced with a solid-state diffusion treatment, and a segregation anneal was performed. The dimensions of the box are $22.5 \times 22.2 \times 19.5$ nm^3 and there are 333,665 atoms in the reconstruction. The matrix Ag atoms have been omitted for the sake of clarity.

After internal oxidation, the random distribution of Mn atoms becomes nonrandom as MnO precipitates are formed. In Fig. 4(a) and (b), we see what appears to be an array of flat, platelet-like shaped precipitates approximately perpendicular to the direction of analysis. In Fig. 4(b), only the matrix atoms are shown along with the isoconcentration surfaces for the sake of clarity. It is clear that within the regions bounded by the isoconcentration surfaces, the density of matrix Ag atoms is reduced.

In Fig. 5, we note the presence of a number of complex ionic species, not present in the group A specimen mass spectrum (Fig. 3), which are associated with the field-evaporation of MnO precipitates (see Table 2). Two items in Table 2 are noteworthy. First, is the presence of an O^+, monatomic oxygen peak. This peak was not observed in the as-cast specimen (see Fig. 3), indicating that the presence of O^+ ions is associated strictly with the field-evaporation of the MnO oxide precipitates. The exclusive association of monatomic, singly-charged oxygen with the field-evaporation of oxide precipitates is a phenomenon that has been observed, though not explicitly mentioned, in our prior atom-probe investigations of ceramic/metal interfaces [8–10, 19–21, 24]. Second, is the presence of a number of complex ionic species including, in order of increasing

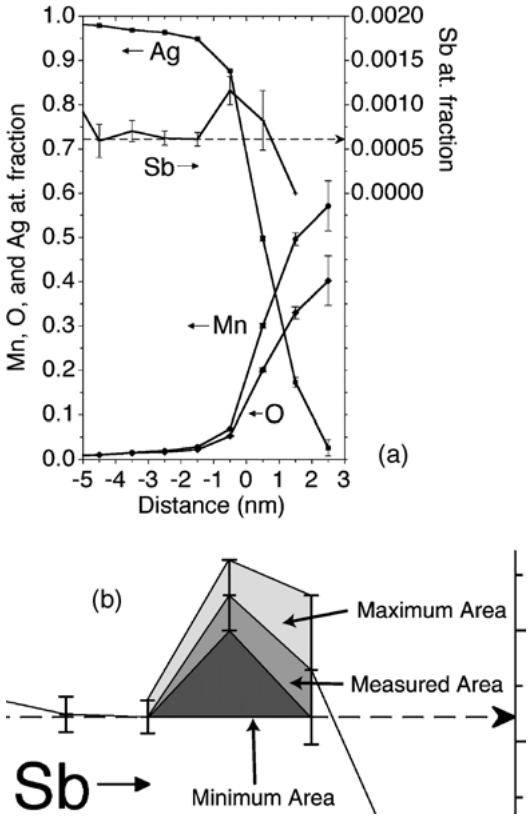

Figure 9. (a) Proxigram showing the Mn, O, Ag and Sb atomic fractions as functions of distance from the surfaces of the precipitates of a group D specimen (see Fig. 8). Negative distances represent regions outside of the isoconcentration surfaces (i.e., matrix), while positive distances represent regions inside of the isoconcentration surfaces (i.e., precipitates). The error bars are large on the rightmost data points due to the limited proxigram bin population for these values of the abscissa. We note an approximately 1:1 stoichiometry within the MnO precipitates. The centers of the precipitates contain, on average, less than 5 at.% Ag. The background level of Sb within the Ag matrix is approximately 0.0006 at.fr. (0.06 at.%). The segregation of Sb at the MnO/Ag ceramic/metal interfaces can be seen clearly in the Sb curve (note the dual axes for the ordinates). (b) Highlight of the Sb curve in (a) showing the segregation of Sb at the MnO/Ag(Sb) interface. The Gibbsian interfacial excess, $\Gamma_{Sb}^{MnO/Ag}$, as extracted from the area of the maximum in the curve, is $(3.8 \pm 2.1) \times 10^{16}$ m^{-2} ($(3.8 \pm 2.1) \times 10^{-2}$ nm^{-2}) at 550°C (see text for details).

mass-to-charge state ratio, MnO^{2+}, $MnO_2{}^{2+}$, $MnO_3{}^{2+}$, $Mn_2\ O^{+}$, MnO^{+}, $MnO_2{}^{+}$, and $MnO_3{}^{+}$ plus their hydrides. The presence of such complex ions is evidence of the complicated conditions occurring during the field-evaporation of ceramic precipitates from within a metal matrix. Further discussion of such complications is found below. A final comment on Table 2: We note that the total number of masses that fall into the indicated windows is 438,274, while the total number of atoms in the reconstructions in Fig. 4(a) and (b) is 347,388. The difference in these two numbers is a direct reflection of the positioning efficiency of the 3DAP (in this case, approximately 80%).

Figure 6 shows a proxigram analysis of Mn, O and Ag atomic concentrations as functions of distance to the isoconcentration surface shown in Fig. 4(b). The power of the proxigram method of analysis is that it samples all of the interfacial area represented by the isoconcentration surface in Fig. 4(b) at once [15]. For each atom in the reconstructions in Fig. 4(a) and (b), the minimum distance of that atom to the nearest portion of an isoconcentration surface in Fig. 4(b) is determined. The atoms are placed in bins according to this minimum distance, and the bins are normalized relative to their individual populations to yield the proxigram shown in Fig. 6.

We find an approximately 1:1 stoichiometry within the MnO precipitates, as anticipated, though the oxygen concentration is somewhat reduced. This reduction of apparent oxygen concentration has been observed in previous atom-probe analyses of ceramic precipitates, and appears to be a characteristic feature of the physics of the field-evaporation of metal oxides contained within a conducting metal matrix [8–10, 19–21, 24]. Aside from being related to complications during the field-evaporation of oxides, the apparent reduction in oxygen may be related to the fact that the singly-charged, monatomic, oxygen peak at a mass-to-charge state ratio of 16 (see Table 2) is, in fact, doubly-charged, diatomic oxygen ($O_2{}^{2+}$). As a result, windowing the peak as a monatomic ion underestimates the oxygen content by a factor of two. There is, unfortunately, no way to account for such a complication, and so the peak is windowed as a monatomic ion. Figure 6 shows that the centers of the MnO precipitates contain, on average, approximately 45–50 at.% Ag, an observation that is discussed further below.

For the group C specimen (internally oxidized with Sb in solid-solution but no segregation anneal), the mass spectrum exhibits essentially all of the same characteristics (that is, peaks) of the group B specimen (see Fig. 5 and Table 2). The only major difference is the presence of singly-charged antimony peaks. Antimony has two stable isotopes, with approximately 50:50 abundance, for the masses 121 and 123; the actual ratio is 1.34 (0.573/0.427). During atom-probe analyses, the antimony ions occur as singly-charged quadruple hydrides, $^{121}SbH_4{}^{+}$ and $^{123}SbH_4{}^{+}$, occurring at

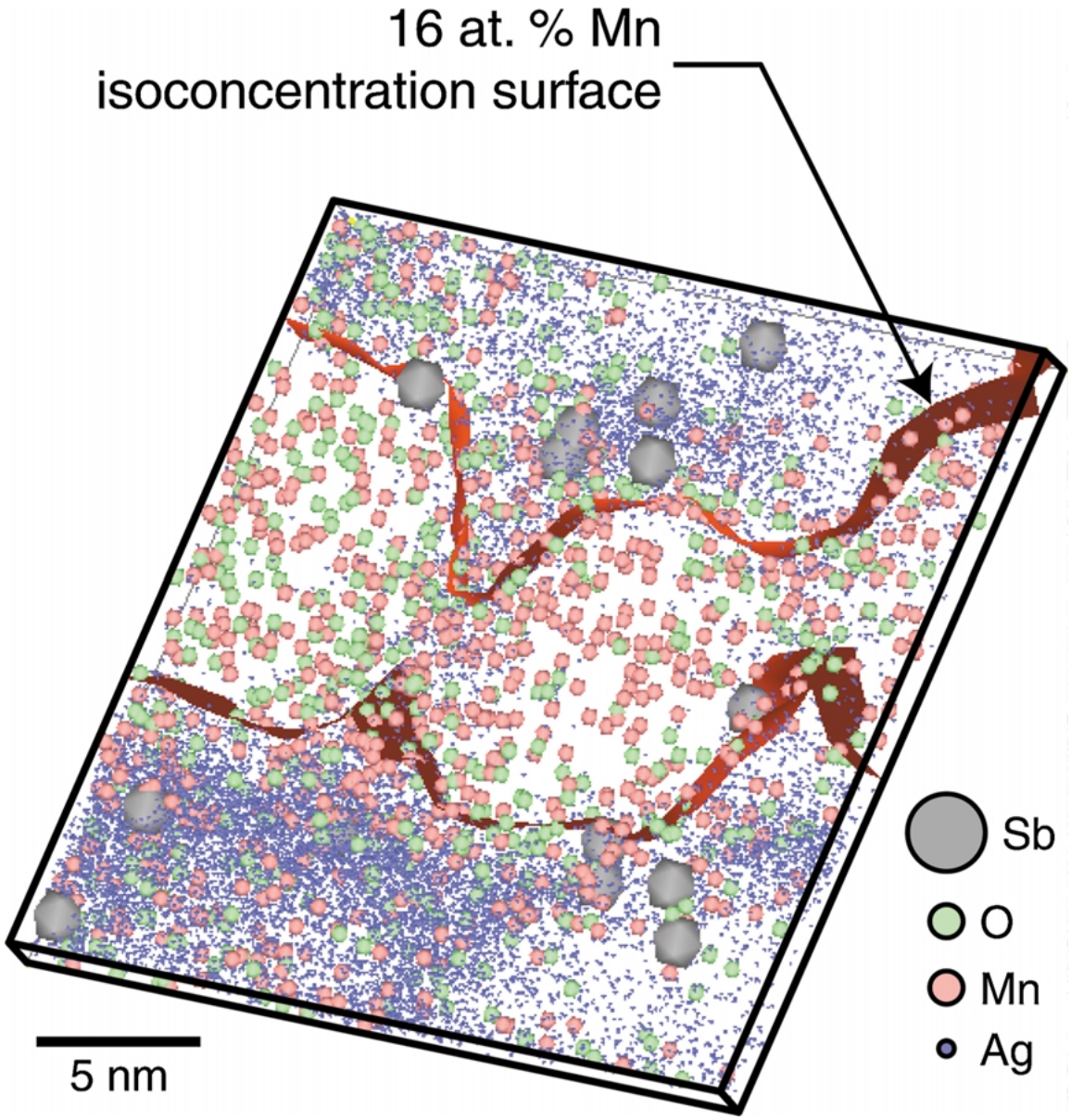

Figure 10. A slice of the 3DAP reconstruction shown in Fig. 9. The slice is taken from approximately the middle of the reconstruction (the thickness of the slice is approximately 1 nm). A 16 at.% Mn isoconcentration surface is overlaid on the data set. We see clearly the distinction between regions of matrix and precipitate. The segregation of Sb atoms in the region near the isoconcentration surface is evident qualitatively. The atomic density difference between precipitate and matrix regions in the slice, as delineated by the isoconcentration surface superimposed on the figure, is also evident.

mass-to-charge state ratios of 125 and 127, respectively. Though these mass-to-charge state ratios are the same as those for $^{107}Ag(H_2O)^+$ and $^{109}Ag(H_2O)^+$, the absence of such peaks in the group A and group B spectra (see Fig. 3 and Table 2) confirms that the peaks do, in fact, correspond to $^{121}SbH_4^+$ and $^{123}SbH_4^+$. The specific mechanism for the exclusive occurrence of antimony in the singly-charged quadruple-hydride form is not well understood.

From Fig. 7 we see that for the group C specimen, as with the group B specimen (Fig. 6), approximately a 1:1 stoichiometry within the MnO precipitates is observed. The antimony concentration shows some slight evidence of segregation at the region corresponding

approximately to the MnO/Ag(Sb) interface (i.e., the data point in Fig. 7 at a distance of +0.5 nm), but taking into account the error bars on the concentration values, the observed segregation cannot be considered to be statistically significant. The relatively large measured Sb concentration at a distance of +2.5 nm also does not correspond to Sb segregation at the MnO/Ag(Sb) interface—the error bars are too large, and the distance corresponds to a region well inside of the MnO precipitates (and well removed from the MnO/Ag(Sb) interface). The background level of Sb within the Ag matrix is approximately 0.0013 at.fr. (0.13 at.%). The centers of the precipitates contain, on average, approximately 35–40 at.% Ag, a level that is somewhat reduced relative to the group B specimen (Fig. 6), indicating that the Ag is leaving the MnO precipitates. The presence of Ag within the precipitates is discussed further below.

4.2. Specimen with Segregation (Group D)

For the group D specimen (Fig. 8), the 3DAP reconstruction appears very similar to that of the group B specimen depicted in Fig. 4(a), except that Fig. 8 shows the presence of large Sb atoms (in gray). In Fig. 9(a), we note evidence for segregation of Sb at the MnO/Ag interface, as represented by the small maximum in the Sb curve in Fig. 9(a) at a distance of −0.5 nm. This distance corresponds exactly to the start of the rise in both the Mn and O concentrations in the proxigram (i.e., to the MnO/Ag(Sb) interface). Recall that the proxigram method is able to quantify simultaneously the segregation of Sb at *all* of the interfacial area (i.e., isoconcentration surfaces) in a 3DAP reconstruction. The Gibbsian interfacial excess of Sb at the MnO/Ag(Sb) interfaces, $\Gamma_{\mathrm{Sb}}^{\mathrm{MnO/Ag}}$, is extracted from the area under this maximum (see Fig. 9(b)) [9, 10, 15] and is:

$$\Gamma_{\mathrm{Sb}}^{\mathrm{MnO/Ag}} = (3.8 \pm 2.1) \times 10^{16}\ \mathrm{m}^{-2} ((3.8 \pm 2.1) \times 10^{-2}\ \mathrm{nm}^{-2}) \text{ at } 550^{\circ}\mathrm{C}. \quad (1)$$

This value is for 550°C because the segregation anneal of the specimen was performed at this temperature (see Table 1). It is obtained by multiplying the value for the area under the maximum in the Sb proxigram (which has units of (at.fr.) × (nm) = nm) by the atomic density of the Ag metal matrix (58.6 atoms nm^{-3}).

We now discuss briefly how the error in the measurement of $\Gamma_{\mathrm{Sb}}^{\mathrm{MnO/Ag}}$ is determined [9]. The proxigram method of extracting the Gibbsian interfacial excess has its sources of error in several different effects. First, and primary, is the uncertainty in the area of the peak in the proxigram itself (see Fig. 9(b)). Other secondary sources of error include uncertainty in the threshold level of the isoconcentration surface used to construct the proxigram, field-evaporation effects in the vicinity of a precipitate/matrix interface, and uncertainty in the atomic density of the reconstruction in the vicinity of a precipitate/matrix interface. These latter three secondary sources of error, however, are thought to be insignificant relative to the primary source of error—the uncertainty in the area of the peak in the proxigram. Using the $-\sigma$ (standard deviation) error bars to calculate the area of the peak in the proxigram in Fig. 9(b) (the minimum area in the figure) and extract the Gibbsian interfacial excess yields a value of $2.28 \times 10^{16}\ \mathrm{m}^{-2}$ at 550°C. Using the data points themselves (the measured area in the figure), a value of $3.83 \times 10^{16}\ \mathrm{m}^{-2}$ at 550°C is obtained. Using the $+\sigma$ error bars (the maximum area in the figure) yields a value of $5.9 \times 10^{16}\ \mathrm{m}^{-2}$ at 550°C. Therefore, an *estimate* of the Gibbsian interfacial excess, including error, is $(3.8 \pm 2.1) \times 10^{16}\ \mathrm{m}^{-2}$ ($(3.8 \pm 2.1) \times 10^{-2}\ \mathrm{nm}^{-2}$) at 550°C, as above.

Further qualitative evidence of Sb segregation at the MnO/Ag(Sb) interfaces can be found by comparing the background levels of Sb in the group C and group D (pre- and post-segregation anneal—see Table 1) specimens. The background level of Sb within the Ag matrix in the group C specimen is approximately 0.0013 at.fr. (0.13 at.%) (see Fig. 7). The background level of Sb within the Ag matrix in the group D specimen is approximately 0.0006 at.fr. (0.06 at.%) (see Fig. 7). Clearly, as the Sb segregates to the MnO/Ag(Sb) interfaces, the background level of Sb within the Ag matrix decreases, indicating a depletion effect.

The measured segregation level, namely $(3.8 \pm 2.1) \times 10^{16}\ \mathrm{m}^{-2}$ ($(3.8 \pm 2.1) \times 10^{-2}\ \mathrm{nm}^{-2}$) at 550°C, is small. Previous 3DAP and 2DAP examinations of segregation at ceramic/metal interfaces have yielded values of the Gibbsian interfacial excess on the order of 10^{17} to $10^{18}\ \mathrm{m}^{-2}$ [8–10, 21]. The small measured value reported in this paper is a testament to the sensitivity of the 3DAP technique for the quantitative investigation of segregation at internal, heterophase interfaces. The value of the Sb concentration data point in Fig. 9(a) at a distance value of −0.5 nm is $(1.159 \pm 0.159) \times 10^{-3}$ at.fr. The error bars are calculated using standard binomial statistics [15]:

$$\sigma = \sqrt{\frac{c_i\,(1 - c_i)}{N}}; \quad (2)$$

where σ is one-standard deviation, c_i is the concentration of component i within the proxigram bin, and N is the total number of atoms in the proxigram bin. Comparison of Eq. (2) with the value of the Sb concentration data point at a distance of -0.5 nm, given above, yields a total proxigram population, N, of 45,792 atoms. A concentration of $(1.159 \pm 0.159) \times 10^{-3}$ at.fr. corresponds, therefore, to 53 ± 7 Sb atoms in this proxigram bin. This value should be compared to the number of Sb atoms expected, based on the measured background concentration of Sb in this specimen. The background level of Sb within the Ag matrix in this specimen is approximately 0.0006 at.fr. (as above), corresponding to 27 Sb atoms within a proxigram bin of this size. The segregation of Sb atoms as measured experimentally is clearly statistically significant. Moreover, the total segregation, as represented by the value $\Gamma_{\mathrm{Sb}}^{\mathrm{MnO/Ag}}$ presented above, is calculated from the total area of the peak in the proxigram (Fig. 9(b)), and not just from the value of the Sb concentration at a distance of -0.5 nm.

A previous quantitative study of Sb segregation at Cu/MnO ceramic/metal interfaces dealt with matrix and interface concentrations of Sb on the order of 5–15 at.% [25]. It is noted, however, that the maximum measured Sb concentration at the interface is on average more than twice as large as the bulk concentration. This is entirely consistent with the values reported in this report. As above, the maximum value of Sb concentration in Fig. 9(a) is $(1.159 \pm 0.159) \times 10^{-3}$ at.fr. (at a distance value of -0.5 nm). The background level of Sb in this specimen is approximately 0.0006 at.fr. The enhancement factor for Sb at the MnO/Ag(Sb) interface is $1.93 \approx 2$, which is comparable to the values reported for the MnO/Cu(Sb) system [25]. Again, the agreement is a testament to the sensitivity of the 3DAP technique for the quantitative investigation of segregation at internal, heterophase interfaces.

4.3. The Driving Force for Segregation

A possible contribution to the driving force for the segregation of Sb at MnO/Ag(Sb) interfaces is related to the elastic strain energy associated with the volume change experienced by a solute atom. This driving force is due to the release of the elastic strain energy associated with an Sb atom in the matrix as a result of interfacial segregation. In terms of atomic volumes, the volume percentage difference between matrix Ag atoms and Sb atoms in solution is approximately 45% [26]. This large volume difference allows for the possibility of some unknown fraction of the solute atom's strain energy to be released at the MnO/Ag(Sb) interfaces due to its segregation at the MnO/Ag interface.

We commence by considering the total amount of elastic strain energy that may be dissipated at an interface arising from the difference in atomic volumes between the solute and the solvent atoms (Sb and Ag, respectively, in this case). This total elastic strain energy, calculated for the case where the solute and solvent atoms have different elastic moduli, is given by [27]:

$$E_{el} = \frac{24\pi r_{\mathrm{solute}}^3 \varepsilon^2 KG}{3K + 4G}; \tag{3}$$

where K is the bulk modulus of the solute, G is the shear modulus of the solvent, and r_{solute} is the radius of the solute atom. The quantity ε, the volume size misfit between the atoms, is defined as:

$$\varepsilon = \frac{r_{\mathrm{solute}}^3 - r_{\mathrm{solvent}}^3}{r_{\mathrm{solvent}}^3}; \tag{4}$$

where r_{solvent} is the radius of the solvent atom. For calculating ε, the Seitz radii are used, as they are determined from atomic volumes [26]. For the elastic moduli, single crystal values at the relevant temperature are used [28]. Values of Eq. (3) are tabulated in Table 3 for the four different ceramic/metal systems we have studied by atom-probe microscopy.

We see from Table 3 that the system with the highest value of total elastic strain energy (MgO/Cu(Sb) at 500°C) is 6.1 eV, and it exhibits the highest experimental value of the Gibbsian interfacial excess, 2.9 nm^{-2}. Aside from this, however, the correlation between total elastic strain energy and the Gibbsian interfacial excess of solute is poor. Some important conclusions, however, can be culled from Table 3. As the MgO/Cu(Sb) at 500°C system has the highest value of both total elastic strain energy and Gibbsian interfacial excess, we can conclude that for this system the release of some of the elastic strain energy contributes to the driving force for segregation. Similarly, as the CdO/Ag(Au) system has a negligible value for total strain energy (1.1×10^{-4} eV) because the Seitz radii for gold and silver are nearly identical (1.594 and 1.598 Å, respectively [26]). Since the CdO/Ag(Au) system also exhibits a significant value for Gibbsian interfacial excess (1.65 nm^{-2}), we conclude that the driving force for segregation has its origin in other physical effects. Analogous conclusions can be drawn for the other two

Table 3. Values of the total amount of elastic strain energy that may be dissipated at an interface arising from the difference in atomic volumes between the solute and the solvent atoms (in this case, the segregating species and the metal matrix, respectively)—see Eq. (3) in the text—and the corresponding value of the Gibbsian interfacial excess (as measured by 3DAP microscopy).

System	Elastic strain energy (eV) (see Eq. (3))	Gibbsian interfacial excess (nm^{-2})	Lattice parameter mismatch[a]
MgO/Cu(Sb) at 500°C	6.1	2.9 [10]	15.0%
MnO/Ag(Sb) at 550°C	1.2	0.038 [this paper]	20.2%
MgO/Cu(Ag) at 500°C	0.47	0.32 [10]	15.0%
CdO/Ag(Au) at 650°C	1.1×10^{-4}	1.65 [9]	14.8%

[a]Lattice mismatch = $\frac{|a_{\text{ceramic}} - a_{\text{metal}}|}{1/2\,(a_{\text{ceramic}} + a_{\text{metal}})}$

systems presented in Table 3. These trends imply that the strain energy associated with an oversized (or undersized atom) is not completely released as a result of its segregation at a ceramic/metal interface. Therefore, the driving force for segregation of a solute atom must have other physical origins.

A more sophisticated analysis of trends in segregation behavior would have to account for factors other than the release of elastic strain energy, Eq. (3). These factors include interfacial energy considerations (where the presence of a segregating impurity atom acts to reduce the interfacial energy of the interface), and chemical considerations [29]. The latter two factors may only be accessible by first principles investigations of the energy of segregation at ceramic/metal interfaces (of the type described in references [30–32]) and/or the approach developed by Legrand, Tréglia et al. for calculating the driving force for surface and grain boundary segregation [33–35].

4.4. Field-Evaporation Complications

The atomic density difference between precipitate and matrix regions in the slice in Fig. 10, as delineated by the isoconcentration surface superimposed on the figure, is evident. Such a density difference is a result of complications in the field-evaporation of ions from the MnO oxide precipitates [8, 10]. Two other observations are evidence for such complications. First, is the presence of complex ionic species in the spectra of the specimens that had been internally oxidized (i.e., groups B, C, and D); see Fig. 5, Table 2, and the discussion above. Second, is the apparent alignment of the MnO precipitates perpendicular to the direction of analysis (see the 3DAP reconstructions in Figs. 4(a), 4(b), and 8).

4.5. Nanoscale Evolution of MnO Precipitates and Para- and Orthoequilibrium

Finally, we discuss the presence of Ag atoms within the MnO precipitates. In Fig. 6 (the group B specimen), we see a background Ag concentration of approximately 45 at.%. In Fig. 7 (the group C specimen), we detect a background Ag level of approximately 35–40 at.%. Finally, in Fig. 9(a) (the group D specimen), we find a Ag concentration level of less than 5 at.% within the MnO precipitates. Clearly, as the specimens underwent successive heat treatments (internal oxidation, the introduction of Sb by solid-state diffusion, and an Sb segregation annealing treatment; see Table 1), the concentration of Ag measured within the MnO precipitates decreases systematically; that is, the MnO precipitates are rejecting the silver atoms they inherited from the matrix. We suggested earlier that the detection of metal matrix ions within ceramic precipitates during atom-probe microscopy analysis may be an artifact of the field-evaporation process [8]. In the present investigation, however, in the group D specimen (see Fig. 9(a)), less than 5 at.% Ag was detected within the MnO precipitates. This observation contradicts the suggestion that the detection of metal matrix ions within metal oxide precipitates during atom-probe microscopy analyses is a phenomenon associated with the field-evaporation process. An explanation for the observed systematic decrease in Ag concentration within the MnO precipitates is that the specimens analyzed in the present investigation were all in different stages of oxide precipitate formation and that the evolution of MnO precipitates involves the continuous, but slow, rejection of Ag from their volume. That is, growth of the nanometer-size precipitates was still occurring, and although the measured stoichiometry of the precipitates is approximately what is anticipated (i.e., 1:1

Mn to O), a considerable remnant Ag concentration remained within the precipitates until the Sb segregation anneal and then it decreased to <5 at.% Ag. This is because the diffusion of oxygen is rapid compared to the diffusion of Ag during the internal oxidation processing step and this step involves paraequilibrium conditions [36], where the diffusivity of silver is small compared with the diffusivity of oxygen. In particular, at the temperature of internal oxidation, 900°C (see Table 1), the ratio of oxygen diffusivity in silver, $D_{\mathrm{Ox}}^{\mathrm{Ag}}$, to silver self-diffusivity, D_{Ag}, is approximately 14,000 [37]. That is, oxygen diffuses in silver many orders of magnitude faster than silver self-diffuses (owing to the fact that oxygen diffuses interstitially in silver [37]), and thus paraequilibrium conditions prevail. With increasing annealing time orthoequilibrium conditions [36] prevail and the MnO precipitates reject the trapped Ag atoms. This is a physically important result because it provides an atomistic picture for the evolution of an oxide precipitate produced by internal oxidation that is quite different from the widely used classical picture envisaged by Wagner [38]. Specifically, our results demonstrate that one can obtain a nearly stoichiometric MnO precipitate, at the internal oxidation temperature, without the rejection of all the silver matrix atoms in the region where it forms.

5. Summary and Conclusions

- The 3DAP analysis of nanometer-size MnO ceramic precipitates embedded in an Ag metal matrix has been presented. Several factors that indicate complex field-evaporation conditions during the analysis of the ceramic precipitates have been identified and discussed. These factors include the apparent density difference between precipitate and matrix regions in the 3DAP reconstructions (see Fig. 10), the presence of complex ionic species in the spectra of the specimens that had been internally oxidized (see Fig. 5 and Table 2), and the apparent alignment of the MnO precipitates perpendicular to the direction of analysis (see Figs. 4(a), 4(b), and 8).
- For specimens containing Sb, introduced via a solid-state diffusion treatment, the segregation of Sb at the MnO/Ag(Sb) ceramic/metal interfaces is quantified in the form of proximity histograms (proxigrams). For the specimen that had not undergone a segregation annealing treatment, no statistically significant segregation was detected. For the specimen that had undergone a segregation anneal at 550°C, statistically significant segregation of Sb at the MnO/Ag(Sb) interfaces is detected. The Gibbsian interfacial excess of Sb at the interface, $\Gamma_{\mathrm{Sb}}^{\mathrm{MnO/Ag}}$, as extracted directly from the proxigram, is $(3.8 \pm 2.1) \times 10^{16}\ \mathrm{m}^{-2}$ ($(3.8 \pm 2.1) \times 10^{-2}\ \mathrm{nm}^{-2}$) at 550°C.
- As the specimens underwent successive heat treatments (internal oxidation, the introduction of Sb by solid-state diffusion, and an Sb segregation anneal; see Table 1), the amount of Ag measured within the MnO precipitates decreased systematically to a value of less than 5 at.%. An explanation for the observed systematic decrease in Ag concentration within the MnO precipitates is that the specimens analyzed in the present investigation were all at the early stages of oxide precipitate formation, while growth was still occurring and that with continued growth of MnO precipitates the concentration of Ag decreased continuously. This is because the diffusion of silver is slow compared to the diffusion of oxygen during all the processing steps (specifically, approximately 14,000 times slower at the temperature of internal oxidation, 900°C). Therefore, during internal oxidation paraequilibrium conditions prevail and with increasing annealing time, in the absence of oxygen, orthoequilibrium conditions are reached and the MnO precipitates reject the Ag matrix atoms they inherited from the matrix under paraequilibrium conditions.

Acknowledgments

This research is supported by the U.S. Department of Energy, Basic Sciences Division. A U.S. Department of Defense Graduate Fellowship partially supported J.T.S. Special thanks are due to Dr. Dieter Isheim for his experimental assistance and useful discussions and Drs. Roy Benedek, John W. Cahn and Gautam Ghosh for useful discussions.

References

1. F. Ernst, Mat. Sci. Eng. **R14**, 97 (1995).
2. B.J. Kooi, A.R. Westers, and J.Th.M. De Hosson, Mat. Sci. Forum **294–296**, 255 (1999).
3. D. Blavette, B. Deconihout, A. Bostel, J.M. Sarrau, M. Bouet, and A. Menand, Rev. Sci. Instrum. **64**, 2911 (1993).
4. A. Cerezo, T.J. Godfrey, S.J. Sijbrandij, G.D.W. Smith, and P.J. Warren, Rev. Sci. Instrum. **69**, 49 (1998).
5. B. Deconihout, C. Pareige, D. Blavette, and A. Menand, Micros. Microanal. **5**, 39 (1999).

6. M.K. Miller and G.D.W. Smith, *Atom Probe Microanalysis: Principles and Applications to Materials Problems* (Materials Research Society, Pittsburgh, 1989).
7. D. Isheim, private communication.
8. J. Rüsing, J.T. Sebastian, O.C. Hellman, and D.N. Seidman, Micros. Microanal. **6**, 445 (2000).
9. J.T. Sebastian, O.C. Hellman, and D.N. Seidman, in *Materials Research Society Proceedings* **654**, AA4.9.1 (2001).
10. J.T. Sebastian, J. Rüsing, O.C. Hellman, D.N. Seidman, W. Vriesendorp, B.J. Kooi, and J.Th.M. De Hosson, Ultramicoscopy **89**, 203 (2001).
11. D. Isheim, R. Csencits, and D.N. Seidman, Mater. Res. Soc. Symp. **652**, Y10.2.1 (2001).
12. D. Isheim, E.J. Siem, and D.N. Seidman, Ultramicroscopy, **89**, 195 (2001).
13. D. Isheim, O.C. Hellman, D.N. Seidman, F. Danoix, A. Bostel, and D. Blavette, Micros. Microanal. **7**, 424 (2001).
14. D. Isheim and D.N. Seidman, Metall. Mater. Trans, **4**, to appear (2002).
15. O.C. Hellman, J.A. Vandenbroucke, J. Rüsing, D. Isheim, and D.N. Seidman, Micros. Microanal. **6**, 437 (2000).
16. W. Vriesendorp, M.S. Thesis, University of Groningen, Groningen, The Netherlands, 2000.
17. E. Sonder, L.M. Slifkin, and C.T. Tomizuka, Phys. Rev. **93**, 97 (1954).
18. J. Crank, *Mathematics of Diffusion* (Oxford University Press, Oxford, 1956).
19. D.K. Chan, Ph.D. Thesis, Northwestern University, Evanston, IL, 1994.
20. D.K. Chan, D.N. Seidman, and K.L. Merkle, Phys. Rev. Lett. **75**, 1118 (1995).
21. D.A. Shashkov, D.A. Muller, and D.N. Seidman, Acta Mater. **47**, 3953 (1999).
22. O.C. Hellman, J.A. Vandenbroucke, J. Blatz du Rivage, and D.N. Seidman, Mater. Sci. Eng. A **327**(1–2) (2002).
23. J.T. Sebastian, O.C. Hellman, and D.N. Seidman, Rev. Sci. Instrum. **72**(7), 2984 (2001).
24. D.A. Shashkov, M.F. Chisholm, and D.N. Seidman, Acta Mater. **47**, 3939 (1999).
25. W. Vriesendorp, B.J. Kooi, and J.Th.M. De Hosson, Scripta Mater. **45**, 169 (2001).
26. H.W. King, J. Mat. Sci. **1**, 79 (1966).
27. P. W. Voorhees and W. C. Johnson, J. Chem. Phys. **84**, 5108 (1986).
28. G. Simmons and H. Wang, *Single Crystal Elastic Constants and Calculated Aggregate Properties: A Handbook* (The M.I.T. Press, Cambridge, MA, 1971).
29. W.C. Johnson and J.M. Blakely, *Interfacial Segregation* (American Society for Metals, Metals Park, OH, 1979).
30. R. Benedek, M. Minkoff, and L.H. Yang, Phys. Rev. B **54**, 7697 (1996).
31. R. Benedek, D.N. Seidman, M. Minkoff, L.H. Yang, and A. Alavi, Phys. Rev. B **60**, 16094 (1999).
32. R. Benedek, A. Alavi, D.N. Seidman, L.H. Yang, D.A. Muller, and C. Woodward, Phys. Rev. Lett. **84**, 3362 (2000).
33. G. Tréglia, B. Legrand, F. Ducastelle, A. Saúl, C. Gallis, I. Meunier, C. Mottet, and A. Senhaji, Comput. Mat. Sci. **15**, 196 (1999).
34. F. Berthier, B. Legrand, and G. Tréglia, Acta Mater. **47**, 2705 (1999).
35. J. Creuze, F. Berthier, R. Tétot, B. Legrand, and G. Tréglia, Phys. Rev. B **61**, 14470 (2000).
36. A. Hultgren, Trans. ASM **39**, 915 (1947); J.S. Kirkaldy, Cand. J. Phys. **36**, 899 (1958); G.R. Purdy, D.H. Weichert, and J.S. Kirkaldy, Trans. AIME **230**, 1025 (1964).
37. W. Eichenhauer and G. Müller, Z. f. Metallkd. **53**, 321 (1962); S.J. Rothmann, N.L. Peterson, and J.T. Robinson, Phys. Status Solidi **39**, 635 (1970).
38. C. Wagner, Z. Elektrochem. **63**, 772 (1959).